Circular dichroism and Faraday and Kerr rotation in two-dimensional materials with intrinsic Hall conductivities

F. R. Pratama,* M. Shoufie Ukhtary, and Riichiro Saito
Department of Physics, Tohoku University, Sendai 980-8578, Japan

(Received 29 October 2019; revised manuscript received 23 December 2019; published 21 January 2020)

The electronic structures of two-dimensional hexagonal materials for a given spin direction can be generally written by the Haldane model, which shows circular dichroism or valley polarization due to broken time-reversal and inversion symmetries, respectively. By using the Kubo formula, we calculate longitudinal and transversal (Hall) optical conductivities to obtain the absorption spectra. The absorption spectra for circularly polarized lights are calculated by solving the Maxwell equations with a boundary conditions at the two-dimensional material. We found that circular dichroism and valley polarization depend on the properties of the imaginary part of the Hall conductivity, while the real part of the Hall conductivity generates large Faraday and Kerr rotations up to a few degrees.

DOI: 10.1103/PhysRevB.101.045426

I. INTRODUCTION

The emergence of graphene in 2004 [1] has paved the way for a trend in physics due to its unusual electronic and transport properties [2]. Research on graphene-based and graphene-like two-dimensional (2D) materials has found more functionalities for possible applications [3]. One of the phenomena which is applicable for optical filters is circular dichroism (CD). Circular dichroism is a property of a material in which the absorption probabilities of left- and right-handed circularly polarized (LCP and RCP, respectively) lights are not equal. Naturally, weak CD is observed in a chiral molecule with lack of mirror symmetries [4,5]. Some nanoscale-based structures have been proposed to enhance CD for practical purposes, including molecule-nanoparticle hybrid [4] and 2D metamaterials [5]. In the latter case, it is experimentally demonstrated that CD occurs due to the difference of the Ohmic (Joule) heating for LCP and RCP lights in the metametarials [5].

In the context of 2D hexagonal materials, CD is observed in silicene [6]. Furthermore, monolayer transition-metal dichalcogenides (TMDs) such as MoS_2 and WSe_2 [7–12] exhibit valley polarization (VP), where electron at the K (K') valley in the Brillouin zone absorbs only LCP (RCP) light. It is known that CD and VP originate from broken time-reversal ($\mathcal{T}$) and inversion ($\mathcal{I}$) symmetries in the 2D hexagonal materials, respectively [6,7], and these two phenomena have been investigated for further advances in optical sensors, valleytronics, and next-generation electronic devices with low-energy consumption [6,9].

A Hamiltonian which breaks the $\mathcal{T}$ and $\mathcal{I}$ symmetries in the honeycomb lattice is generally provided by the Haldane model [13], which was originally proposed as a model that exhibits quantum Hall effect without an external magnetic field, and the pioneering model for topological insulators [14,15]. Hence, the Haldane model can be a starting point for theoretical investigations of CD and VP in the 2D hexagonal materials. Furthermore, Jotzu *et al.* [16] have experimentally realized a system with the Haldane Hamiltonian using cold atoms modulated in optical lattice. The topological Haldane materials are also predicted to occur in Fe-based ferromagnetic insulators [17]. A recent theoretical study of the optical absorption in the Haldane model has been performed by Ghalamkari *et al.* [18], in which they show within dipole approximation that the Haldane material exhibits perfect CD (i.e., the material only absorbs either LCP or RCP light), which is independent of VP. However, the absorption spectra generally depend on the frequency of light and angle of incidence, which can be obtained by solving the Maxwell equations with a boundary conditions at the 2D material, which is the subject of this paper. Here we investigate the roles of the intrinsic Hall conductivity in the in the optical absorption of the Haldane model. This approach provides not only a better understanding of CD and VP in the 2D hexagonal materials but also the prediction of the Faraday and Kerr rotations in the remaining transmitted and reflected lights.

A phenomenon which occurs in the transmission (reflection) of light due to the Hall conductivity is the Faraday (Kerr) rotation. In the Faraday (Kerr) rotation, the polarization plane of incident linearly polarized light (which is given by the sum of LCP and RCP lights) is rotated after the transmission (reflection), while the transmitted (reflected) light acquires ellipticity. In the presence of an external magnetic field, Crassee *et al.* [19] observe giant Faraday rotation ($\sim 6^\circ$) in graphene, which is attributed to the cyclotron resonance and inter-Landau-level transitions. Shimano *et al.* [20] experimentally demonstrate that the quantum Hall effect in graphene also plays a decisive role in large Faraday and Kerr rotations. Huang *et al.* [21] utilize the magneto-optical Kerr effect to detect ferromagnetism in monolayer CrI_3. Theoretically, Széchenyi *et al.* [22] predict that large Faraday and Kerr

*pratama@flex.phys.tohoku.ac.jp

rotations (up to few degrees) can occur for bilayer graphene in a quantum anomalous Hall state without the magnetic field. Hence, it is meaningful to examine the Faraday and Kerr rotations in the Haldane model as a generalized Hamiltonian of the 2D hexagonal materials.

Here we calculate the longitudinal and transversal (Hall) conductivities of the Haldane model as a function of the frequency of light, which are derived from the Kubo formula. In particular, we show that the Hall conductivity without the external magnetic field in the Haldane model is crucial for the absorption spectra of circularly polarized light. By obtaining the optical conductivities, we solve the absorption probabilities of LCP and RCP lights using the Maxwell equations. We found that the imaginary part of the Hall conductivity is responsible for the occurrence of CD and VP. We also calculate the ellipticity and the Faraday (Kerr) angle of the transmitted (reflected) light, in which we show that the ellipticity is proportional to CD and that the real part of the Hall conductivity generates large Faraday and Kerr rotations up to a few degrees.

The paper is organized as follows. In Sec. II, analytical methods for calculating the optical conductivities and the absorption for circularly polarized lights are given. In Sec. III, calculated results are shown. In Sec. IV, a conclusion is given.

II. CALCULATION METHODS

A. The Haldane Hamiltonian

The Hamiltonian of the Haldane model in the 2D hexagonal lattice can be expressed by

$$\hat{\mathcal{H}} = -t_1 \sum_{\langle i,j\rangle} c_i^\dagger c_j + t_2 \sum_{\langle\langle i,j\rangle\rangle} e^{i\nu_{ij}\phi} c_i^\dagger c_j + M \sum_i \tau_i c_i^\dagger c_i, \quad (1)$$

where $c_i^\dagger(c_i)$ is the creation (annihilation) operator of the ith atomic site. The first term in the Hamiltonian denotes the nearest-neighbor (NN) interactions with the hopping integral $t_1 > 0$. The second term is the next-nearest-neighbor (NNN) interactions with the hopping integral $t_2 > 0$, which breaks the $\mathcal{T}$ symmetry for a nonzero phase angle ϕ in $e^{i\nu_{ij}\phi}$. Here we take $\nu_{ij} = +1$ (-1) for clockwise (anticlockwise) NNN hopping direction [13], as illustrated in Fig. 1(a). In the third term, we define $\tau_i = +1$ (-1) for the A (B) sublattice, which denotes on-site energy difference for the A $(+M)$ and B $(-M)$ sublattices. This breaks the $\mathcal{I}$ symmetry between A and B atoms and gives rise to the band gap $2M$ between the valence and conduction bands at the K and K' points in the Brillouin zone, as shown in Fig. 1(b).

By performing the Fourier transform of Eq. (1), we calculate the energy dispersion in the Brillouin zone. Since we are interested in low-energy excitation, we define the effective Hamiltonian around the K and K' points. The first-order expansion of the Hamiltonian near the K and K' points can be expressed in term of 2×2 unit matrix $\hat{\sigma}_0$ and the Pauli matrices $\hat{\sigma}_x$, $\hat{\sigma}_y$, $\hat{\sigma}_z$ as follows [15,23]:

$$\hat{\mathcal{H}}(\mathbf{q}) = (-3t_2\cos\phi)\hat{\sigma}_0 + \hbar v_F(\kappa q_x\hat{\sigma}_x + q_y\hat{\sigma}_y) + (M - \kappa 3\sqrt{3}t_2\sin\phi)\hat{\sigma}_z, \quad (2)$$

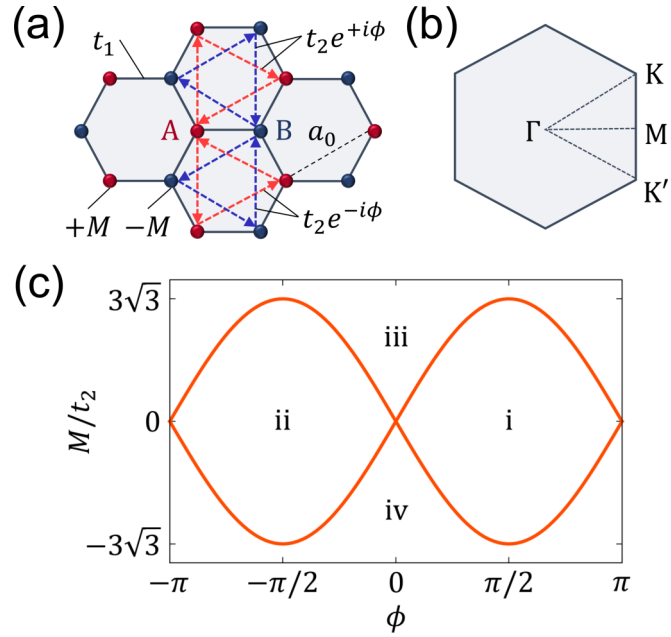

FIG. 1. (a) The Haldane model on the 2D hexagonal lattice with A and B sublattices and lattice constant a_0. The strength of the NN hopping is given by t_1. The complex NNN hopping is expressed by $t_2e^{+i\phi}$ $(t_2e^{-i\phi})$ for the clockwise (anticlockwise) direction. The on-site energy for A (B) sublattice is $+M$ $(-M)$. (b) The Brillouin zone of the 2D hexagonal lattice with symmetry points. (c) Phase diagram of the Haldane model. The topological (band) insulator phase is denoted by i and ii (iii and iv).

where $\mathbf{q} = (q_x, q_y)$ is the wave vector of electron measured from the K and K' points. The valley index κ is given by $+1$ (-1) for the K (K') point and v_F is the Fermi velocity, which is defined by $v_F \equiv \sqrt{3}t_1a_0/(2\hbar)$. It is known that the topological phase occurs when $|M/t_2| < 3\sqrt{3}|\sin\phi|$; otherwise, the material is a band (or trivial) insulator [13–15]. In the phase diagram of the Haldane model, the topological (band) insulator is given in regions i and ii (iii and iv) as shown in Fig. 1(c). By solving the energy dispersion from Eq. (2), we calculate the optical conductivities whose properties depend on the regions in the phase diagram of the Haldane model.

B. The Kubo formula for optical conductivity

By using the Kubo formula, the optical conductivity σ_{ij}, $(i, j = x, y)$ as a function of the frequency of light ω and momentum $\mathbf{k}$ in the 2D systems is given by [24,25]:

$$\sigma_{ij}(\mathbf{k},\omega) = -ie^2\hbar \int \frac{d^2\mathbf{q}}{(2\pi)^2} \sum_{b,b'} \frac{f[\epsilon_b(\mathbf{q})] - f[\epsilon_{b'}(\mathbf{q}+\mathbf{k})]}{\epsilon_b(\mathbf{q}) - \epsilon_{b'}(\mathbf{q}+\mathbf{k})} \times \frac{\langle b,\mathbf{q}|\hat{v}_i|b',\mathbf{q}+\mathbf{k}\rangle\langle b',\mathbf{q}+\mathbf{k}|\hat{v}_j|b,\mathbf{q}\rangle}{\epsilon_b(\mathbf{q}) - \epsilon_{b'}(\mathbf{q}+\mathbf{k}) + \hbar\omega + i\hbar\gamma}, \quad (3)$$

where $\epsilon_{b(b')}$ is the electron energy of the band $b(b')$ which is the eigenvalue of Eq. (2) and $f[\epsilon_{b(b')}]$ is the Fermi distribution function. The velocity operator in the direction of i, $\hat{v}_i$ $(i = x, y)$ is defined by

$$\hat{v}_i \equiv \frac{1}{\hbar}\frac{\partial\hat{\mathcal{H}}}{\partial q_i}. \quad (4)$$

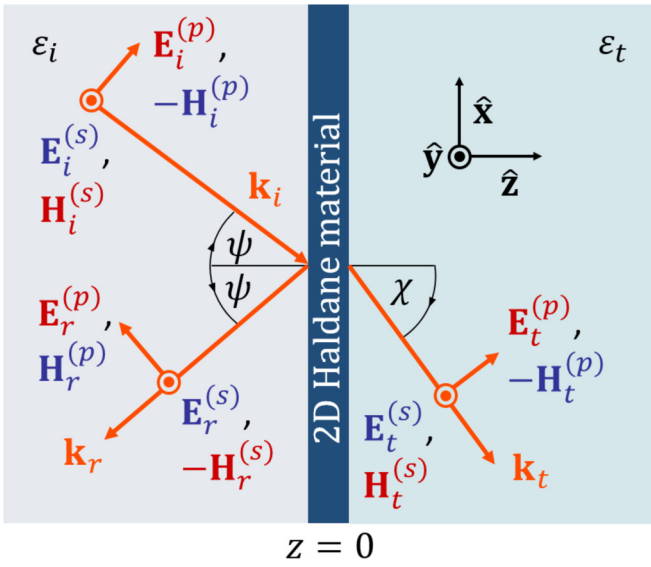

FIG. 2. The electric and magnetic fields in the system consisting of the 2D Haldane material between two dielectric media, whose relative permittivities are ε_i and ε_t. The angles of incidence and transmission are given by ψ and χ, respectively. The red (blue) color in the electric and magnetic fields depend on p_m (s'_m).

Since we focus our attention for the optical transition, we can take $\mathbf{k} \to \mathbf{0}$ measured from the K (or K' point). It is also assumed that the damping constant $\gamma \to 0$, which means that the scattering due to impurity in the Haldane material is neglected for simplicity.

C. The Maxwell boundary conditions with the Hall conductivity

In Fig. 2, we show the geometry for calculating transmission, reflection, and absorption probabilities. In the calculation, the 2D Haldane material is placed between two dielectric media in the xy plane at $z = 0$, while the xz plane is the plane of incidence for the electromagnetic wave. The relative permittivity of the medium for the incident (transmitted) light is denoted by ε_i (ε_t). The incident light comes with angle of incidence ψ and is refracted by angle χ, which satisfies the Snell law $\sqrt{\varepsilon_i}\sin\psi = \sqrt{\varepsilon_t}\sin\chi$. Any electric field $\mathbf{E}_m$ can be written as a sum of independent electric fields with p polarization $\mathbf{E}_m^{(p)}$ and s polarization $\mathbf{E}_m^{(s)}$, as follows:

$$\mathbf{E}_m = \mathbf{E}_m^{(p)} + \mathbf{E}_m^{(s)} = E_m^{(p)}\hat{\mathbf{p}}_m + E_m^{(s)}\hat{\mathbf{s}}_m, \tag{5}$$

where $m = i,\ t,$ and r indicate the incident, transmitted, and reflected lights, respectively, and $\hat{\mathbf{p}}_m$ ($\hat{\mathbf{s}}_m$) is the unit vector in the direction of the p (s) component. We can express $E_m^{(p)} = E_0 p_m$ and $E_m^{(s)} = E_0 s_m e^{i\Phi_m}$, where Φ_m is the phase difference between the p- and s-polarized lights. The electric field can be represented by the Jones vector as follows:

$$\mathbf{E}_m = E_0\begin{pmatrix} p_m \\ s_m e^{i\Phi_m}\end{pmatrix} = E_0\begin{pmatrix} p_m \\ s'_m\end{pmatrix}, \tag{6}$$

hence, the electric field amplitude is given by $E_0\sqrt{|p_m|^2 + |s'_m|^2}$. To make sure that the incident light has the magnitude of E_0, p_i and s'_i are chosen to satisfy $|p_i|^2 + |s'_i|^2 = 1$. In particular, for incident LCP (RCP) light, $\Phi_i = +\pi/2$ $(-\pi/2)$, $p_i = 1/\sqrt{2}$ $(1/\sqrt{2})$, and $s'_i = +i/\sqrt{2}$ $(-i/\sqrt{2})$.

The p and s components of the magnetic fields are related to the electric fields by the following ratios:

$$H_m^{(s)} = \frac{E_m^{(p)}}{Z_m}, \quad H_m^{(p)} = \frac{E_m^{(s)}}{Z_m}, \tag{7}$$

where Z_m is the impedance of electromagnetic wave. Z_m is given by the relative permittivity ε_m as $Z_m = Z_0/\sqrt{\varepsilon_m}$ and $Z_0 = 376.73\ \Omega$ is the impedance of vacuum. Therefore $H_m^{(s)}$ ($H_m^{(p)}$) is proportional to p_m (s_m). The directions of the electric fields $\mathbf{E}_m^{(p)}$, $\mathbf{E}_m^{(s)}$ and magnetic fields $\mathbf{H}_m^{(s)}$, $\mathbf{H}_m^{(p)}$ are illustrated in Fig. 2.

The boundary conditions at $z = 0$ are obtained from $\nabla \times \mathbf{E} = -\mu\partial\mathbf{H}/\partial t$ and $\nabla \times \mathbf{H} = \mathbf{J} + \varepsilon\partial\mathbf{E}/\partial t$, where μ, ε, and $\mathbf{J}$ are permeability, permittivity, and surface current density, respectively. The boundary conditions are given by

$$E_i^{(p)}\cos\psi + E_r^{(p)}\cos\psi = E_t^{(p)}\cos\chi, \tag{8}$$

$$H_t^{(s)} - \left[H_i^{(s)} - H_r^{(s)}\right] = -\left[\sigma_{xx}(\omega)E_t^{(p)}\cos\chi + \sigma_{xy}(\omega)E_t^{(s)}\right], \tag{9}$$

$$E_i^{(s)} + E_r^{(s)} = E_t^{(s)}, \tag{10}$$

and

$$-H_t^{(p)}\cos\chi - \left[-H_i^{(p)}\cos\psi + H_r^{(p)}\cos\psi\right] = \sigma_{yy}(\omega)E_t^{(s)} + \sigma_{yx}(\omega)E_t^{(p)}\cos\chi. \tag{11}$$

From Eqs. (8)–(11), it is noted that the s and p components of the electric field are mixed each other for nonzero σ_{xy} and σ_{yx}.

By expressing the dependence of the electric fields $E_m^{(p)}$ and $E_m^{(s)}$ as well as the magnetic fields $H_m^{(p)}$ and $H_m^{(s)}$ in Eqs. (8)–(11) in terms of p_m and s'_m, we have

$$p_i\cos\psi + p_r\cos\psi = p_t\cos\chi, \tag{12}$$

$$\frac{p_i}{Z_i} - \frac{p_r}{Z_i} = p_t\left[\frac{1}{Z_t} + \sigma_{xx}(\omega)\cos\chi\right] + s'_t\sigma_{xy}(\omega), \tag{13}$$

$$s'_i + s'_r = s'_t, \tag{14}$$

and

$$s'_i\frac{\cos\psi}{Z_i} - s'_r\frac{\cos\psi}{Z_i} = s'_t\left[\frac{\cos\chi}{Z_t} + \sigma_{yy}(\omega)\right] + p_t\sigma_{yx}(\omega)\cos\chi. \tag{15}$$

Let us define a variable ξ_m as the ratio of s'_m and p_m as follows:

$$\xi_m \equiv \frac{s'_m}{p_m}. \tag{16}$$

In the case of LCP (RCP) lights, $\xi_m = +i$ $(-i)$, while for a linearly polarized light, we can take $\xi_m \to 0$. The transmission and reflections probabilities, T and R, are given by

$$T = \frac{\frac{1}{2}\mathrm{Re}[\mathbf{E}_t \times \mathbf{H}_t^*]\cdot(+\mathbf{z})}{\frac{1}{2}\mathrm{Re}[\mathbf{E}_i \times \mathbf{H}_i^*]\cdot(+\mathbf{z})} = \frac{|p_t|^2(1+|\xi_t|^2)}{|p_i|^2(1+|\xi_i|^2)}\frac{Z_i\cos\chi}{Z_t\cos\psi}, \tag{17}$$

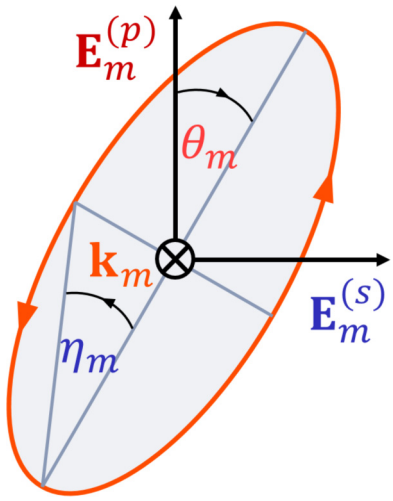

FIG. 3. An elliptically polarized light with independent basis $\mathbf{E}_m^{(p)}$ and $\mathbf{E}_m^{(s)}$. The angles of polarization rotation and ellipticity are given by ψ_m and η_m, respectively.

and

$$R = \frac{\frac{1}{2}\mathrm{Re}[\mathbf{E}_r \times \mathbf{H}_r{}^*] \cdot (-\mathbf{z})}{\frac{1}{2}\mathrm{Re}[\mathbf{E}_i \times \mathbf{H}_i{}^*] \cdot (+\mathbf{z})} = \frac{|p_r|^2(1+|\xi_r|^2)}{|p_i|^2(1+|\xi_i|^2)}, \tag{18}$$

respectively. Because of the nonzero optical conductivities, a fraction of the light is absorbed by the 2D Haldane material. The absorption probability A is given by

$$A = 1 - R - T. \tag{19}$$

In Fig. 3, an elliptically polarized light is depicted as an ellipse in the $[E_m^{(p)}, E_m^{(s)}]$ coordinate. The circular and linear polarizations of light are the special cases of elliptical polarization. The elliptically polarized lights are parametrized by angles θ_m and η_m, which are the rotation of the polarization plane and the ellipticity, respectively. Hence, for the linearly p-polarized light, we have $\theta_m = 0$ and $\eta_m = 0$, while for the circularly polarized lights we have $\theta_m = 0$ and $\eta_m = +\pi/4$ (LCP) or $\eta_m = -\pi/4$ (RCP). The angles θ_m and η_m are related to the phase difference between $\mathbf{E}_m^{(p)}$ and $\mathbf{E}_m^{(s)}$, Φ_m [26,27], and can be expressed as a function of ξ_m as follows:

$$\tan(2\theta_m) = \frac{2\mathrm{Re}[\xi_m]}{1-|\xi_m|^2}, \tag{20}$$

and

$$\sin(2\eta_m) = \frac{2\mathrm{Im}[\xi_m]}{1+|\xi_m|^2}. \tag{21}$$

In the next section, we calculate the ellipticity of the transmitted and reflected lights as well as the Faraday and Kerr rotations by using Eqs. (20) and (21).

III. RESULTS

A. Optical conductivities of the Haldane material

The low-energy dispersion of the Haldane model [eigenvalue of Eq. (2)] is given by

$$\epsilon(\mathbf{q}) = -3t_2\cos\phi \mp \sqrt{|\hbar v_F \mathbf{q}|^2 + (M - \kappa 3\sqrt{3}t_2\sin\phi)^2}, \tag{22}$$

where the sign $-$ $(+)$ corresponds to valence (conduction) band. The energy dispersions at the valence band ϵ_v and the conduction band ϵ_c are related by $\epsilon_v + 3t_2\cos\phi = -(\epsilon_c + 3t_2\cos\phi)$, and the energy gap at the K ($\kappa = +1$) and K' points ($\kappa = -1$) is given by $\epsilon_g^{(\kappa)} \equiv 2|M - \kappa 3\sqrt{3}t_2\sin\phi|$. It is noted that the energy gaps for the K and the K' points have different values when the $\mathcal{T}$ and the $\mathcal{I}$ symmetries are simultaneously broken ($t_2 \neq 0$, $\phi \neq 0$, and $M \neq 0$).

By solving the eigenvectors of Eq. (2), the matrix elements of velocity are calculated as follows:

$$\begin{aligned}\langle v, \mathbf{q}+\mathbf{k}|\hat{v}_x|v, \mathbf{q}\rangle &= -\kappa v_F \frac{\left[(\epsilon_c+\zeta)^2 - {\Gamma_\kappa}^2\right]^{1/2}}{\epsilon_c+\zeta}\cos\left(\frac{\varphi}{\kappa}\right) \\ &= -\langle c, \mathbf{q}+\mathbf{k}|\hat{v}_x|c, \mathbf{q}\rangle,\end{aligned} \tag{23}$$

$$\begin{aligned}\langle v, \mathbf{q}+\mathbf{k}|\hat{v}_y|v, \mathbf{q}\rangle &= -v_F \frac{\left[(\epsilon_c+\zeta)^2 - {\Gamma_\kappa}^2\right]^{1/2}}{\epsilon_c+\zeta}\sin\left(\frac{\varphi}{\kappa}\right) \\ &= -\langle c, \mathbf{q}+\mathbf{k}|\hat{v}_y|c, \mathbf{q}\rangle,\end{aligned} \tag{24}$$

$$\begin{aligned}\langle c, \mathbf{q}+\mathbf{k}|\hat{v}_x|v, \mathbf{q}\rangle &= \kappa v_F\left[\cos\left(\frac{\varphi}{\kappa}\right) + i\frac{\Gamma_\kappa}{\epsilon_c+\zeta}\sin\left(\frac{\varphi}{\kappa}\right)\right] \\ &= \langle v, \mathbf{q}|\hat{v}_x|c, \mathbf{q}+\mathbf{k}\rangle^*,\end{aligned} \tag{25}$$

and

$$\begin{aligned}\langle c, \mathbf{q}+\mathbf{k}|\hat{v}_y|v, \mathbf{q}\rangle &= v_F\left[\sin\left(\frac{\varphi}{\kappa}\right) - i\frac{\Gamma_\kappa}{\epsilon_c+\zeta}\cos\left(\frac{\varphi}{\kappa}\right)\right] \\ &= \langle v, \mathbf{q}|\hat{v}_y|c, \mathbf{q}+\mathbf{k}\rangle^*,\end{aligned} \tag{26}$$

where we define $\zeta \equiv 3t_2\cos\phi$, $\Gamma_\kappa \equiv M - \kappa 3\sqrt{3}t_2\sin\phi$, and $\varphi \equiv \arctan(q_y/q_x)$.

The optical conductivity σ_{ij} consists of intraband (Drude) conductivity $\sigma_{ij}^{(D,\kappa)}$ and interband conductivity $\sigma_{ij}^{(E,\kappa)}$ from the K and K' valleys as follows:

$$\sigma_{ij} = \sum_{\kappa=+1,-1}\left[\sigma_{ij}^{(D,\kappa)} + \sigma_{ij}^{(E,\kappa)}\right]. \tag{27}$$

Hereafter, we restrict our calculations for low temperature ($T \approx 0$ K). The intraband (interband) conductivity originates from the transition of electron within the same (between different) band(s). In the case of the Fermi energy $\epsilon_F \geqslant 0$, the longitudinal and Hall intraband conductivities of the κ valley are given by

$$\begin{aligned}\sigma_{xx}^{(D,\kappa)}(\omega) &= \frac{e^2}{4\hbar}\frac{(\epsilon_F+\zeta)^2 - {\Gamma_\kappa}^2}{(\epsilon_F+\zeta)}\delta(\hbar\omega)\Theta\left[\epsilon_F - \epsilon_{c0}^{(\kappa)}\right] \\ &\quad + i\frac{e^2}{4\pi\hbar^2\omega}\frac{(\epsilon_F+\zeta)^2 - {\Gamma_\kappa}^2}{(\epsilon_F+\zeta)}\Theta\left[\epsilon_F - \epsilon_{c0}^{(\kappa)}\right] \\ &= \sigma_{yy}^{(D,\kappa)}(\omega)\end{aligned} \tag{28}$$

and

$$\sigma_{xy}^{(D,\kappa)}(\omega) = -\sigma_{yx}^{(D,\kappa)}(\omega) = 0, \tag{29}$$

where $\epsilon_{c0}^{(\kappa)} \equiv -3t_2\cos\phi + |M - \kappa 3\sqrt{3}t_2\sin\phi|$ as the bottom of the conduction band of the K or K' valley. Hence, $\sigma_{xx}^{(D,\kappa)}$ has nonzero value if only $\epsilon_F > \epsilon_{c0}^{(\kappa)}$. On the other hand, the intraband Hall conductivity $\sigma_{xy}^{(D,\kappa)}$ is always zero even though the $\mathcal{T}$ symmetry is broken, because the product

$\langle b,\mathbf{q}|\hat{v}_x|b,\mathbf{q}+\mathbf{k}\rangle\langle b,\mathbf{q}+\mathbf{k}|\hat{v}_y|b,\mathbf{q}\rangle$ [see Eqs. (23) and (24)] is an odd function $\sim\cos(\varphi/\kappa)\sin(\varphi/\kappa)$ with respect to φ.

The interband conductivities of the K or K' valley are given as follows:

$$\begin{aligned}\sigma_{xx}^{(E,\kappa)}(\omega) &= \frac{e^2}{16\hbar}\left[1+\frac{4{\Gamma_\kappa}^2}{(\hbar\omega)^2}\right]\Theta[\hbar\omega-2(\Lambda_\kappa+\zeta)]\\ &\quad+i\frac{e^2}{16\pi\hbar}\left[1+\frac{4{\Gamma_\kappa}^2}{(\hbar\omega)^2}\right]\ln\left|\frac{2(\Lambda_\kappa+\zeta)-\hbar\omega}{2(\Lambda_\kappa+\zeta)+\hbar\omega}\right|\\ &\quad+i\frac{e^2}{4\pi\hbar^2\omega}\frac{{\Gamma_\kappa}^2}{(\Lambda_\kappa+\zeta)}\\ &= \sigma_{yy}^{(E,\kappa)}(\omega),\end{aligned}\tag{30}$$

and

$$\begin{aligned}\sigma_{xy}^{(E,\kappa)}(\omega) &= \frac{e^2}{4\pi\hbar^2\omega}\kappa\Gamma_\kappa\ln\left|\frac{2(\Lambda_\kappa+\zeta)-\hbar\omega}{2(\Lambda_\kappa+\zeta)+\hbar\omega}\right|\\ &\quad-i\frac{e^2}{4\pi\hbar^2\omega}\kappa\Gamma_\kappa\Theta[\hbar\omega-2(\Lambda_\kappa+\zeta)]\\ &= -\sigma_{yx}^{(E,\kappa)}(\omega),\end{aligned}\tag{31}$$

where the function $\Lambda_\kappa\equiv\max[\epsilon_F,\epsilon_{c0}^{(\kappa)}]$ takes the larger value between ϵ_F and $\epsilon_{c0}^{(\kappa)}$. Here, the interband Hall conductivity is nonzero because the imaginary part of the product $\langle b,\mathbf{q}|\hat{v}_x|b',\mathbf{q}+\mathbf{k}\rangle\langle b',\mathbf{q}+\mathbf{k}|\hat{v}_y|b,\mathbf{q}\rangle$ [see Eqs. (25) and (26)] does not vanish after the integration with respect to φ. It can be checked that in the case when the $\mathcal{T}$ and the $\mathcal{I}$ symmetries are conserved ($t_2=0$, $\phi=0$, and $M=0$), the optical conductivities of the monolayer graphene [28,29] are recovered from Eqs. (28)–(31).

From Eq. (31), it is noted that the sign of the real and imaginary parts of $\sigma_{xy}^{(E,\kappa)}$, $\mathrm{Re}[\sigma_{xy}^{(E,\kappa)}]$ and $\mathrm{Im}[\sigma_{xy}^{(E,\kappa)}]$, depend on the region of the phase diagram of the Haldane model as given by Fig. 1(c), since $\sigma_{xy}^{(E,\kappa)}$ consists the factor $\kappa\Gamma_\kappa=\kappa M-3\sqrt{3}t_2\sin\phi$. In region i (ii), where the effect of the broken $\mathcal{T}$ symmetry is dominant over the broken $\mathcal{I}$ symmetry ($|M|<3\sqrt{3}|t_2\sin\phi|$), $\mathrm{Re}[\sigma_{xy}^{(E,\kappa)}]$ and $\mathrm{Im}[\sigma_{xy}^{(E,\kappa)}]$ are positive (negative) for both the K and K' valleys. On the other hand, when the effect of the broken $\mathcal{I}$ symmetry is larger than the broken $\mathcal{T}$ symmetry ($|M|>3\sqrt{3}|t_2\sin\phi|$), $\mathrm{Re}[\sigma_{xy}^{(E,\kappa)}]$ and $\mathrm{Im}[\sigma_{xy}^{(E,\kappa)}]$ are negative for K the valley and positive for the K' valley for region iii and vice versa for region iv.

Let us illustrate the dependence of the optical conductivities on t_2, ϕ, and M for two distinct cases. In the first case we adopt $t_2=0.05$ eV, $\phi=\pi/2$, and $M=0$, while for the second case we adopt $t_2=0.05$ eV, $\phi=0$, and $M=0.5$ eV. Hereafter, we call the first and the second cases topological and trivial cases, respectively. The topological (trivial) case corresponds to region i (iii) in Fig. 1(c). In Fig. 4(a), we show the energy dispersions of the topological and the trivial cases at the K valley, where the energy gaps are $\epsilon_g^{(+1)}=6\sqrt{3}t_2=0.52$ eV and $\epsilon_g^{(+1)}=2M=1$ eV, respectively. The energy dispersions at those of the K' valley are the same.

Let us calculate the optical conductivities in the Haldane model. In Fig. 4(b), we plot $\sigma_{xx}(\omega)$ and $\sigma_{xy}(\omega)$ for the topological case with $\epsilon_F=0$, where only interband transition contributes to the optical conductivities. In the inset of Fig. 4(b), we plot the case for the electron-doped system ($\epsilon_F=0.5$ eV) to illustrate the contribution of intraband transition. It is noted that the σ_{xx} and σ_{xy} consist of the contributions of the electrons at the K and K' valleys, as shown in Eq. (27). We observe that for $\epsilon_F=0$, $\mathrm{Re}[\sigma_{xx}]$ and $\mathrm{Im}[\sigma_{xy}]$ decrease monotonically when $\hbar\omega>\epsilon_g^{(\kappa)}=0.52$ eV, while $\mathrm{Im}[\sigma_{xx}]$ and $\mathrm{Re}[\sigma_{xy}]$ show logarithmic singularities at $\hbar\omega=\epsilon_g^{(\kappa)}$ due to the interband transition. For $\epsilon_F=0.5$ eV, we can see that the $\mathrm{Re}[\sigma_{xx}]$ peaks at $\hbar\omega=0$ and $\mathrm{Im}[\sigma_{xx}]$ has $1/\omega$ dependence at small photon energy, due to the intraband transition. The effect of the electron doping also shifts the singular points of σ_{xx} and σ_{xy} from $\hbar\omega=\epsilon_g^{(\kappa)}$ to $\hbar\omega=2\epsilon_F=1$ eV.

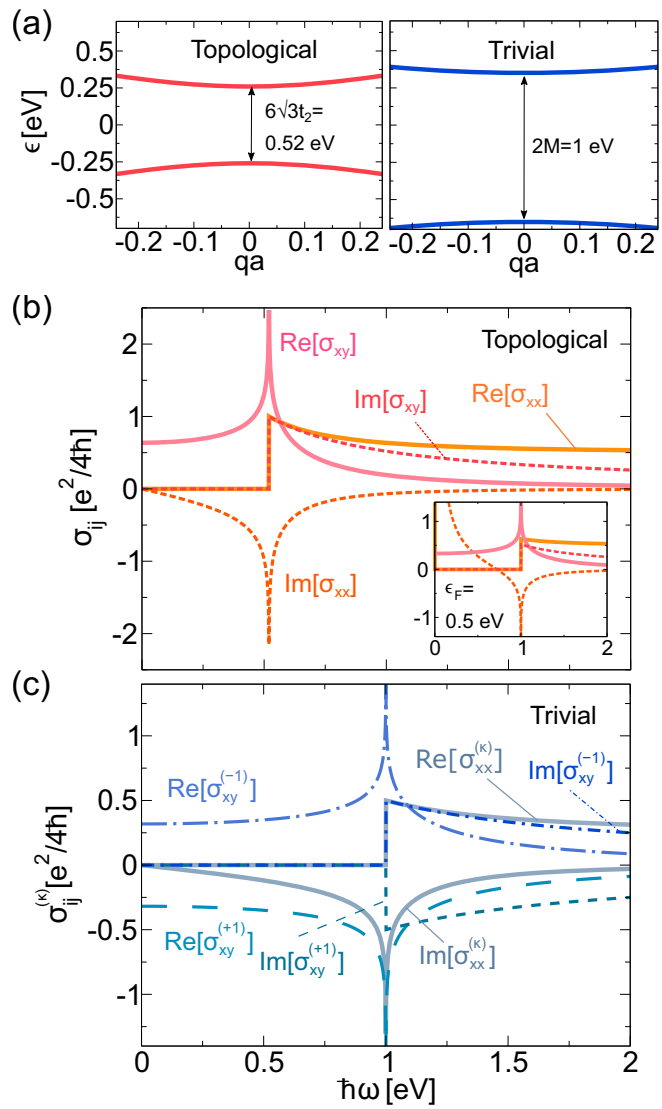

FIG. 4. (a) The energy bands around the K point for the topological ($t_2=0.05$ eV, $\phi=\pi/2$, and $M=0$) and the trivial ($t_2=0.05$ eV, $\phi=0$, and $M=0.5$ eV) cases. (b) The longitudinal and Hall conductivities of the topological case ($\epsilon_F=0$). Inset: The optical conductivities for electron-doped system ($\epsilon_F=0.5$ eV), in which the intraband longitudinal conductivity is nonzero. (c) The longitudinal and the Hall conductivities per valley for the trivial case ($\epsilon_F=0$).

In Fig. 4(c), we plot the optical conductivities per valley $\sigma_{ij}^{(\kappa)}(\omega) \equiv \sigma_{ij}^{(D,\kappa)}(\omega) + \sigma_{ij}^{(E,\kappa)}(\omega)$ for the trivial case ($\epsilon_F = 0$) with $\epsilon_F = 0$. We can see that $\sigma_{xx}^{(\kappa)}$ does not have valley dependence, while the Hall conductivities of electron at the K valley $\sigma_{xy}^{(+1)}$ has equal magnitude but opposite sign of that at the K' valley, $\sigma_{xy}^{(-1)}$. The singularities in the Hall conductivities occur when the light energy match to the energy gap $\hbar\omega = \epsilon_g^{(\kappa)} = 1$ eV.

We shall show that the properties of the optical conductivities in the topological and the trivial cases correspond to CD and VP, respectively, by calculating the optical absorptions for the circularly polarized lights, which is discussed in the next subsection.

B. Optical absorptions in the 2D Haldane material

The variable ξ_m in Eq. (16) for $m = t$ (r) can be obtained by eliminating p_r (p_t) in Eqs. (12) and (13) and s_r' (s_t') in Eqs. (14) and (15) as follows:

$$\xi_t = \frac{\xi_i \Delta_p + Z_i Z_t \sigma_{xy} \cos\chi}{\Delta_s - \xi_i Z_i Z_t \sigma_{xy} \cos\psi}, \tag{32}$$

and

$$\xi_r = \xi_i \frac{\Delta_p + Z_i Z_t \cos\psi \sigma_{xy} \xi_t}{\Delta_p' - Z_i Z_t \cos\psi \sigma_{xy} \xi_t} \frac{\Delta_s' + Z_i Z_t \cos\chi \sigma_{xy}/\xi_t}{\Delta_s - Z_i Z_t \cos\chi \sigma_{xy}/\xi_t}, \tag{33}$$

where Δ_p, Δ_s, Δ_p', and Δ_s' depend on the longitudinal conductivity $\sigma_{xx}(\omega)$ which are defined as follows:

$$\Delta_p \equiv Z_t \cos\chi + Z_i \cos\psi + Z_i Z_t \cos\psi \cos\chi \sigma_{xx}, \tag{34}$$

$$\Delta_s \equiv Z_t \cos\psi + Z_i \cos\chi + Z_i Z_t \sigma_{xx}, \tag{35}$$

$$\Delta_p' \equiv Z_t \cos\chi - Z_i \cos\psi - Z_i Z_t \cos\psi \cos\chi \sigma_{xx}, \tag{36}$$

and

$$\Delta_s' \equiv Z_t \cos\psi - Z_i \cos\chi - Z_i Z_t \sigma_{xx}. \tag{37}$$

For a given ψ and ξ_i, the absorption probability A can be calculated by substituting Eqs. (32) and (33) into Eqs. (17)–(19). For circularly polarized lights ($p_i = 1$, $s_i = \pm 1$, $\xi_i = \pm i$), A is the sum of one-half absorption for p-polarized light A_p and one-half absorption for s-polarized light A_s, as follows:

$$A = \frac{1}{2}A_p + \frac{1}{2}A_s, \tag{38}$$

where A_p and A_s are given by

$$A_p = \frac{4Z_i {Z_t}^2 \cos\psi \cos\chi \mathrm{Re}[\sigma_{xx}\cos\chi + \xi_t \sigma_{xy}]}{|\Delta_p + \xi_t Z_i Z_t \cos\psi \sigma_{xy}|^2} \tag{39}$$

and

$$A_s = \frac{4Z_i {Z_t}^2 \cos\psi \mathrm{Re}[\sigma_{xx} - \sigma_{xy}\cos\chi/\xi_t]}{|\Delta_s - Z_i Z_t \sigma_{xy}\cos\chi/\xi_t|^2}. \tag{40}$$

In the case of normal incidence ($\psi = 0$), we get that $\Delta_p = \Delta_s$ and $\Delta_p' = \Delta_s'$, and from Eqs. (32) and (33), $\xi_t = \xi_r = \xi_i$, which means that the transmitted and reflected lights remain circularly polarized. In such case that $A_p = A_s$, A reduces to

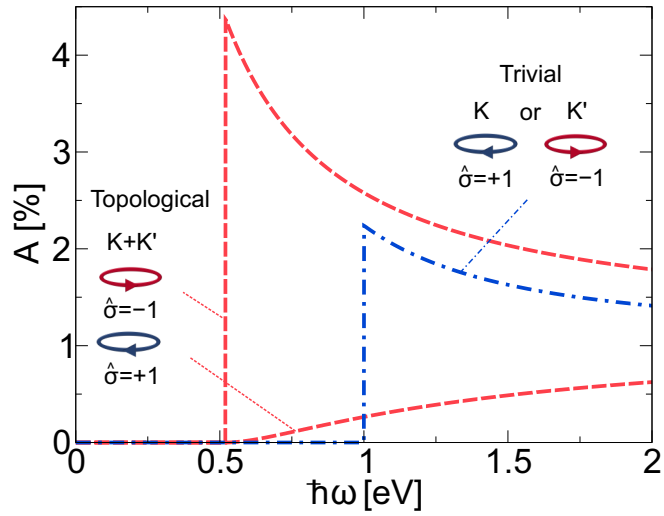

FIG. 5. The optical absorptions of LCP and RCP lights in the topological ($t_2 = 0.05$ eV, $\phi = \pi/2$, and $M = 0$) and the trivial ($t_2 = 0.05$ eV, $\phi = 0$, and $M = 0.5$ eV) Haldane materials with $\epsilon_F = 0$. The former (later) exhibits CD (VP).

A_c, which is given as follows:

$$A_c = \frac{4Z_i {Z_t}^2 \mathrm{Re}(\sigma_{xx} + i\hat{\sigma}\sigma_{xy})}{|Z_i + Z_t + Z_i Z_t(\sigma_{xx} + i\hat{\sigma}\sigma_{xy})|^2} = \frac{4Z_i {Z_t}^2 [\mathrm{Re}(\sigma_{xx}) - \hat{\sigma}\,\mathrm{Im}(\sigma_{xy})]}{|Z_i + Z_t + Z_i Z_t(\sigma_{xx} + i\hat{\sigma}\sigma_{xy})|^2}, \tag{41}$$

where $\hat{\sigma} = +1$ ($\hat{\sigma} = -1$) for LCP (RCP) light. Therefore, for the normal incident, the absorption spectra for circularly polarized lights are proportional to $\mathrm{Re}[\sigma_{xx}]$ and $\mathrm{Im}[\sigma_{xy}]$.

In Fig. 5, we plot the absorption spectra of LCP and RCP lights for the two cases of the Haldane model discussed above. Here we choose $\epsilon_F = 0$, $\psi = 0$, and $\varepsilon_i = \varepsilon_t = 1$. The absorptions for the topological case ($t_2 = 0.05$ eV, $\phi = \pi/2$, and $M = 0$) are shown by the dashed line. We can see that at $\hbar\omega = \epsilon_g^{(\kappa)} = 0.52$ eV, the material only absorbs the RCP light ($\hat{\sigma} = -1$). This corresponds to the perfect CD in the topological Haldane material, which is consistent with the previous result [18]. However, it should be emphasized that even though perfect CD for RCP occurs, the absorption probability for RCP remains low (~4.4%). When the light energy $\hbar\omega$ increases, the absorption for RCP (LCP) light monotonically decreases (increases), and thus CD almost disappears for $\hbar\omega \gg 2$ eV. It is also noted that in the case of $\phi = -\pi/2$, the absorption spectra of RCP and LCP are reversed, because the sign of $\mathrm{Im}[\sigma_{xy}^{(2)}]$ changes to negative.

The optical absorption for the trivial case ($t_2 = 0.05$ eV, $\phi = 0$, and $M = 0.5$ eV) is shown by the dashed-and-dotted line in Fig. 5. Here LCP and RCP lights are absorbed at the K and the K' valleys, respectively, when $\hbar\omega \geqslant \epsilon_g^{(\kappa)} = 1$ eV. This absorption spectrum indicates the occurrence of VP, which can be reversed (i.e., LCP and RCP are absorbed at the K' and the K valleys, respectively) by choosing $M < 0$, because the imaginary part of the Hall conductivity is positive for the K valley and negative for the K' valley. In general, the positive (negative) $\mathrm{Im}[\sigma_{xy}^{(E,\kappa)}]$ corresponds to larger absorption for RCP (LCP), which is shown by Eq. (41).

Before continuing the discussion, let us interpret the macroscopic meaning of CD. In a study by Harada *et al.* [30], it is shown that A in a thin conductor is proportional to the Joule heat,

$$Q = \tfrac{1}{2}\mathrm{Re}[\mathbf{J}\cdot\mathbf{E}_h^*], \tag{42}$$

where $\mathbf{J}$ and $\mathbf{E}_h$ are the electric field and surface current density on the conductor material, respectively. By referring to Fig. 2, $\mathbf{E}_h$ and $\mathbf{J}$ are given as follows:

$$\mathbf{J} = \left[\sigma_{xx}E_t^{(p)}\cos\chi + \sigma_{xy}E_t^{(s)}\right]\hat{\mathbf{x}} + \left[\sigma_{yx}E_t^{(p)}\cos\chi + \sigma_{yy}E_t^{(s)}\right]\hat{\mathbf{y}}, \tag{43}$$

and

$$\mathbf{E}_h = \cos\psi\left[E_i^{(p)} + E_r^{(p)}\right]\hat{\mathbf{x}} + \left[E_i^{(s)} + E_r^{(s)}\right]\hat{\mathbf{y}}. \tag{44}$$

In the case of $\psi = 0$ and $\xi_i = \pm i$, the Joule heat is given by

$$Q = \frac{2{Z_t}^2[\mathrm{Re}(\sigma_{xx}) - \hat{\sigma}\,\mathrm{Im}(\sigma_{xy})]}{|Z_i + Z_t + Z_iZ_t(\sigma_{xx} + i\hat{\sigma}\sigma_{xy})|^2}{E_0}^2. \tag{45}$$

By comparing Eq. (45) with Eq. (41), we can see $A_c = 2Z_iQ/{E_0}^2$, which means that the absorption probability is proportional to the Joule heat in the 2D Haldane material. Therefore, the perfect CD for RCP [as shown by Fig. 5(c) for the topological case] corresponds to the absence of the Joule heat for LCP and vice versa. We have shown that the broken $\mathcal{T}$ symmetry is macroscopically manifested in the difference of Q for LCP and RCP lights (due to σ_{xy}), which is the origin of CD. This phenomenon can be compared with the case of the 2D metamaterials. Khanikaev *et al.* [5] observe that LCP and RCP lights generate different amount of the Joule heat in the asymmetric 2D metamaterial, which is attributed to the origin of CD.

C. Application of the Haldane model in silicene and monolayer TMDs

In this subsection, we will apply the Haldane model to explain CD and VP in silicene and monolayer TMDs. We shall show that by simply changing the Haldane parameters t_2, ϕ, and M, we are able to calculate the optical conductivities and absorption for a given electronic state in the 2D hexagonal materials.

Silicene is a 2D material in which Si atoms are arranged in honeycomb lattice or, in another words, a silicone analog of graphene. However, silicene has a buckled structure, in which the sublattices A and B are separated vertically by a distance 2ℓ ($\ell = 0.23$ Å) [6,31]. By applying an external electric field perpendicular to the silicene plane E_z, a staggered potential between A and B sublattices is generated. Furthermore, Si atom is heavier than C atom, thus, the spin-orbit coupling in silicene ($\lambda_{\mathrm{SO}} = 3.9$ meV) [6,32] is significantly larger compared with that of graphene ($\lambda_{\mathrm{SO}} = 1.3$ μeV) [32] and should be included in the Hamiltonian. The energy dispersion of silicene around the K and K' points [33] is given by

$$\epsilon(\mathbf{q}) = \mp\sqrt{|\hbar v_F\mathbf{q}|^2 + (e\ell E_z - \kappa s\lambda_{\mathrm{SO}})^2}, \tag{46}$$

where $v_F = \sqrt{3}a_0t_1/(2\hbar)$, $a_0 = 3.86$ Å, $t_1 = 1.6$ eV [6]. The spin index s is $+1$ (-1) for spin-up (spin-down) electron.

By substituting $t_2 = \lambda_{\mathrm{SO}}/3\sqrt{3}$, $M = e\ell E_z$, and $\phi = +\pi/2$ ($\phi = -\pi/2$) in the energy dispersion of the Haldane model [Eq. (22)], the state of spin-up (spin-down) electron in silicene as given by Eq. (46) is reproduced. This is similar to the Kane-Mele model in the case of $M = 0$, which takes account the spin-orbit interaction in graphene [14,23,34,35]. From Eq. (46), it can be seen that the energy gap in silicene can be tuned by E_z, which also determines whether silicene is a topological or a band insulator [6]. The transition from the topological phase to the band insulator phase occurs at critical electric field $E_{\mathrm{cr}} = \lambda_{\mathrm{SO}}/e\ell$ [6]. In other words, silicene is a topological (band) insulator when E_z is less (greater) than E_{cr}. Hereafter, the two cases are referred as the topological and insulating cases, respectively. Ezawa [6] has proposed a method to detect the phase transition in silicene by the optical absorption. Within the dipole approximation, it was shown that the absorption spectra in the topological and the insulating silicene obey different spin and valley selection rules. Here we demonstrate that such a phenomenon can be explained by the role of the Hall conductivity in the optical absorption. We can calculate Hall conductivity of silicene per spin and the absorption of circularly polarized lights using Eqs. (28)–(31) and Eq. (41).

First, let us consider the topological silicene by setting $E_z = \lambda_{\mathrm{SO}}/2e\ell < E_{\mathrm{cr}}$. In Fig. 6(a), we plot the energy dispersion at the K and K' valleys for both $s = +1$ and $s = -1$. At the K (K') valley, the electronic band gap for spin-up is smaller (greater) than that of spin-down. In Fig. 6(b), we plot the real and imaginary parts of $\sigma_{xx}(\omega)$, which does not depend on the spin index. In the spectra of $\mathrm{Re}[\sigma_{xx}]$ and $\mathrm{Im}[\sigma_{xx}]$, there are two peaks at different photon energies $\hbar\omega$. The lower-energy peak corresponds to the interband transitions of spin-up electron at the K valley and spin-down electron at the K' valley. The higher energy peak corresponds to the transitions of spin-down electron at the K valley and spin-up electron at the K' valley. In Fig. 6(c), we plot the real and imaginary parts of $\sigma_{xy}(\omega)$ for each spin direction, where the signs of $\mathrm{Re}[\sigma_{xy}]$ and $\mathrm{Im}[\sigma_{xy}]$ are positive for $s = +1$ and negative for $s = -1$. The states $s = +1$ and $s = -1$ belong to regions i and ii in Fig. 1(c), respectively. In Fig. 6(d) we plot the absorption spectra of LCP ($\hat{\sigma} = +1$) and RCP ($\hat{\sigma} = -1$) lights for both $s = +1$ and $s = -1$, where we can distinguish the two spectra. The absorption spectra for RCP light of spin-up and spin-down are given by a solid line and a dashed line, respectively. Here the absorption of spin-up is larger than that of spin-down. In the case of LCP light, the absorption of a given spin is opposite to the RCP light, where the absorption of spin-down (solid line) is higher than that of spin-up (dashed-line). Therefore, the absorption of the circularly polarized light in this case is only determined by the spin index and does not depend on the valley degree of freedom. This phenomenon is known as the spin-selective CD [6]. It is important to note that CD does not occur in the topological silicene, in the sense that the material absorbs RCP and LCP lights with the equal intensity. In other words, the topological silicene is a combination of the topological Haldane phases in region i (for spin-up) and region ii (for spin-down) in the phase diagram of the Haldane model. However, the occurrence of CD in the topological silicene is possible if the number of spin-up and spin-down electrons are not equal.

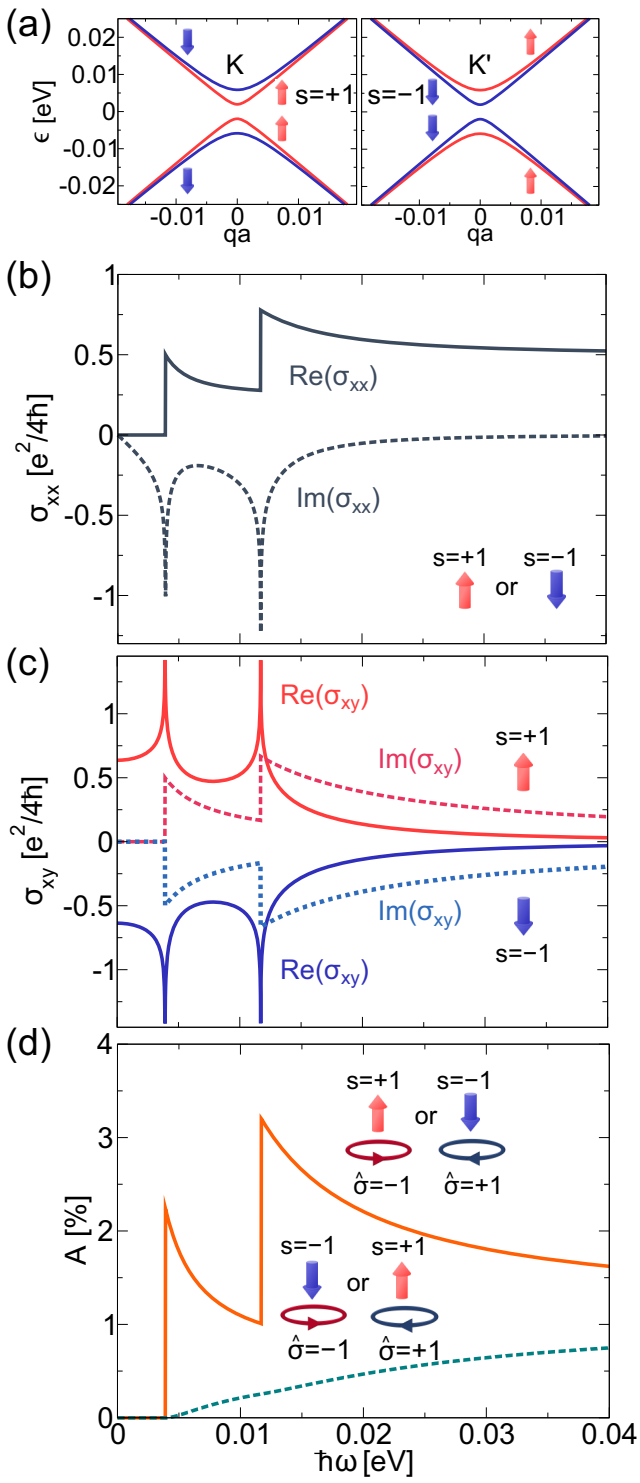

FIG. 6. (a) The electronic energy dispersion of the topological silicene ($e\ell E_z = \lambda_{SO}/2 = 1.95$ meV) at the K and K' valleys. The real and imaginary parts of (b) $\sigma_{xx}(s = \pm 1)$ and (c) σ_{xy} ($s = +1$ and $s = -1$) with the given parameters. (d) The optical absorptions of LCP ($\hat{\sigma} = +1$) and RCP ($\hat{\sigma} = -1$) lights in the topological silicene ($\epsilon_F = 0$, $\psi = 0$, $\varepsilon_i = \varepsilon_t = 1$).

Theoretically, this condition can be realized by introducing magnetic impurities in the system [14,36]. In fact, Kim *et al.* [17] suggested that the topological Haldane material can be synthesized in the form of Fe-based ferromagnetic insulators in a honeycomb lattice, in which electrons in occupied bands are fully polarized in one spin direction owing to the strong Hund coupling in Fe.

Next, we consider the insulating silicene by choosing $E_z = 2\lambda_{SO}/e\ell > E_{cr}$. In Fig. 7(a), we plot the electronic energy dispersions of the spin-up and spin-down electrons at the K and K' valleys, which are similar to that of the topological silicene. The real and imaginary parts of $\sigma_{xx}(\omega)$ are plotted in Fig. 7(b). Here again, we can see two singular peaks of $\mathrm{Re}[\sigma_{xx}]$ and $\mathrm{Im}[\sigma_{xx}]$ originate from the interband transitions of electrons. In Fig. 7(c), we plot the real and imaginary parts of $\sigma_{xy}(\omega)$ for $s = +1$ and $s = -1$, where the signs of $\mathrm{Re}[\sigma_{xy}]$ and $\mathrm{Im}[\sigma_{xy}]$ of each spin direction are opposite at two singular points. For the spin-up electron, $\mathrm{Re}[\sigma_{xy}]$ and $\mathrm{Im}[\sigma_{xy}]$ are negative (positive) at the first (second) excitation energy, which are opposite sign in the case of the spin-down electron. This can be understood by the fact that the first and second peaks correspond to the excitation of the spin-up (spin-down) electrons at the K and K' (K' and K) valleys, respectively. This condition corresponds to region iii in Fig. 1(c), as previously discussed. In Fig. 6(d) we plot the absorption spectra of LCP ($\hat{\sigma} = +1$) and RCP ($\hat{\sigma} = -1$) lights for each spin. The dashed line in Fig. 7(d) corresponds to the absorption of LCP light by the spin-up electron (at the K valley) or RCP light by the spin-down electron (at the K' valley), while the solid line corresponds to the absorption of RCP light by the spin-up electron (at the K' valley) or LCP light by the spin-down electron (at the K valley). Hence the absorption of the circularly polarized lights is only determined by the valley index and not by the spin direction, which indicates the occurrence of VP.

In the case of monolayer TMDs such as MoS_2 and WSe_2, we have a direct band gap due to the broken $\mathcal{I}$ symmetry, since the unit cell consists of one transition-metal atom and two chalcogenide atoms [7,8]. The d orbital of the metal contributes to the spin-orbit interaction, which leads to a strong valley-spin coupling [8]. The energy dispersion at the K and K' valleys is given by [9,37]:

$$\epsilon(\mathbf{q}) = \frac{\kappa s \lambda_{TMD}}{2} \mp \sqrt{|\hbar v_F \mathbf{q}|^2 + \left(\frac{\Delta}{2} - \frac{\kappa s \lambda_{TMD}}{2}\right)^2}. \quad (47)$$

In particular, for monolayer MoS_2 the Fermi velocity of electron $v_F = a_0 t_1/\hbar$, with $a_0 = 3.193$ Å and $t_1 = 1.1$ eV. The energy band gap between valence and conduction bands are $\Delta = 1.66$ eV, and the spin-splitting of energy band at the top of valence band is given by $2\lambda_{TMD} = 0.15$ eV. By adjusting $t_2 = \lambda_{TMD}/3\sqrt{3}$, $M = \Delta/2$, and $\phi = +5\pi/6$ $(-\pi/6)$ in Eq. (22), we reproduce the electronic state of MoS_2 [Eq. (47)] for $s = +1$ ($s = -1$) at the K valley. Similarly for the electron at the K' valley, we choose $\phi = +\pi/6$ $(-5\pi/6)$ to reproduce $s = +1$ ($s = -1$). Therefore, as in the case of silicene, an electronic state in the monolayer MoS_2 can be represented by a particular phase angle in the Haldane model ϕ.

In Fig. 8(a) we plot the energy dispersion of spin-up and spin-down electrons at the K and K' valleys. We can see the splitting of energy band between spin-up and spin-down electrons at the valence bands. At the K valley, the upper (lower) valence band is occupied by spin-up (spin-down) electrons, which is the opposite of that of the K' valley.

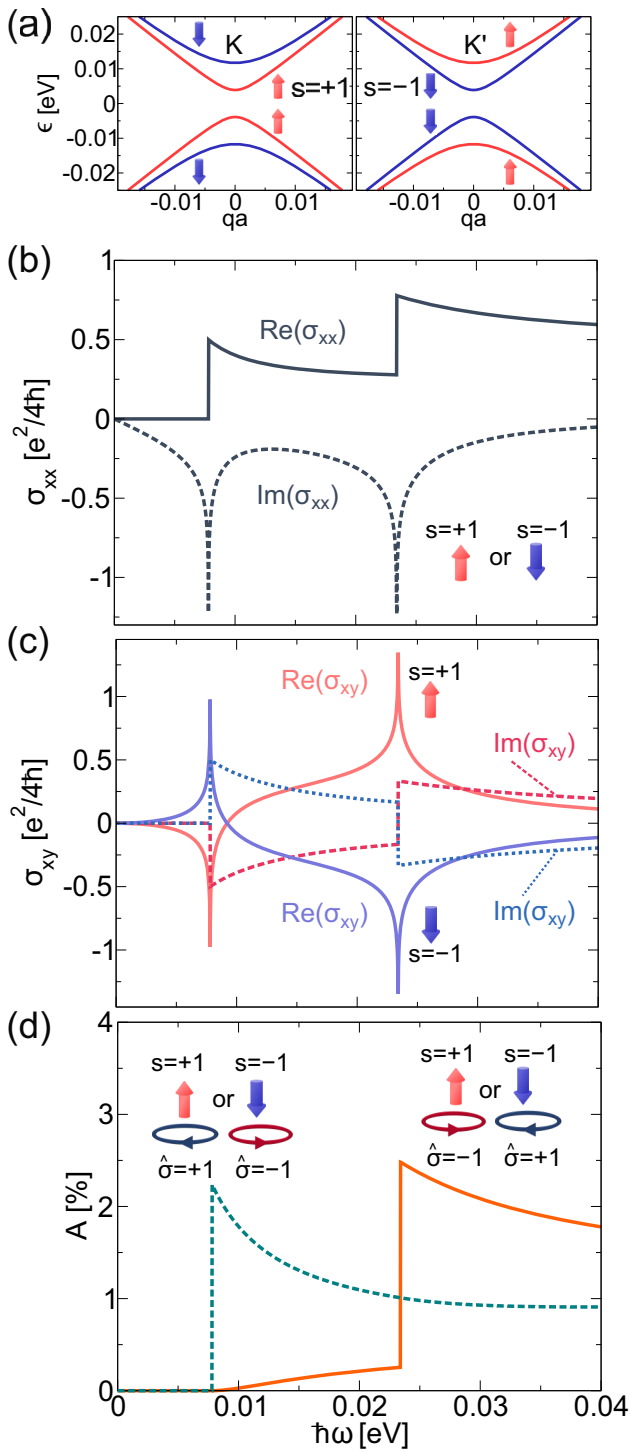

FIG. 7. (a) The electronic energy dispersion of the insulating silicene ($e\ell E_z = 2\lambda_{\rm SO} = 7.8$ meV) at the K and K' valleys. The real and imaginary parts of (b) σ_{xx} ($s = \pm 1$) and (c) σ_{xy} ($s = +1$ and $s = -1$) with the given parameters. (d) The optical absorption of LCP ($\hat{\sigma} = +1$) and RCP ($\hat{\sigma} = -1$) lights in the insulating silicene ($\epsilon_F = 0$, $\psi = 0$, $\varepsilon_i = \varepsilon_t = 1$).

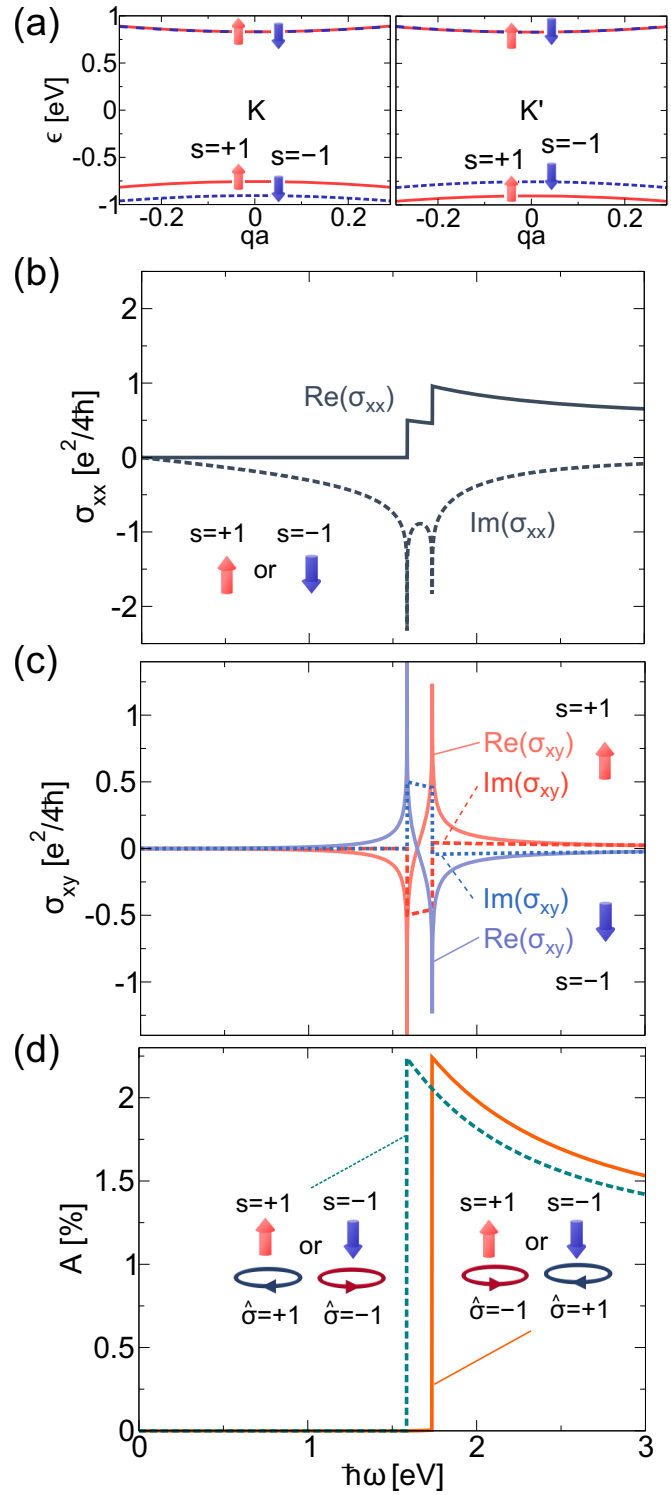

FIG. 8. (a) The electronic energy dispersion of monolayer MoS_2 at the K and K' valleys. The real and imaginary parts of (b) σ_{xx} ($s = \pm 1$) and (c) σ_{xy} ($s = +1$ and $s = -1$) with the given parameters. (d) The optical absorption of LCP ($\hat{\sigma} = +1$) and RCP ($\hat{\sigma} = -1$) lights in the monolayer MoS_2 ($\epsilon_F = 0$, $\psi = 0$, $\varepsilon_i = \varepsilon_t = 1$).

The conduction bands are degenerate at the both valleys. In Fig. 8(b), the real and imaginary parts $\sigma_{xx}(\omega)$ are shown. Here the two singular points are separated by $\hbar\omega = 2\lambda_{\rm TMD}$. In Fig. 8(c), we show Re[σ_{xy}] and Im[σ_{xy}] for each spin which change signs at the two different singular points, as in the case of the insulating silicene. In Fig. 8(d) we plot the absorption spectra for LCP ($\hat{\sigma} = +1$) and RCP ($\hat{\sigma} = -1$) lights for each spin. The RCP light is absorbed by the spin-down and the

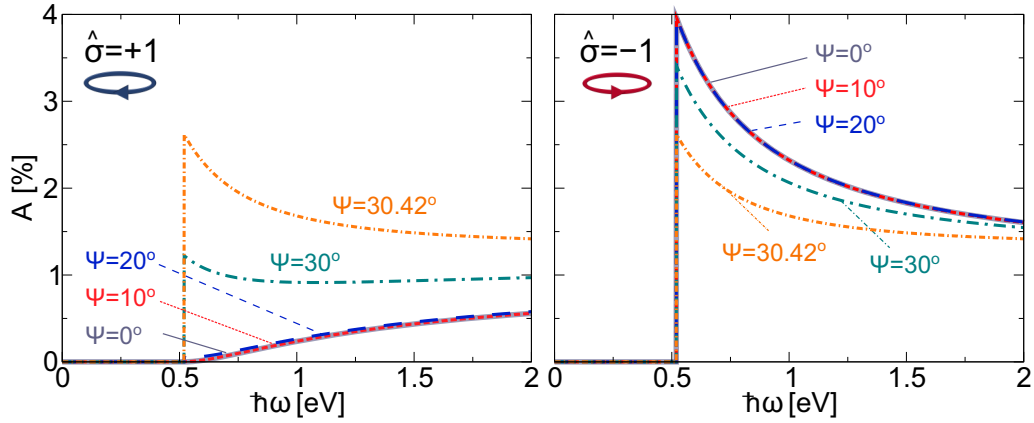

FIG. 9. The absorption probability A for LCP ($\hat{\sigma} = +1$) and RCP ($\hat{\sigma} = -1$) lights in the 2D Haldane material ($t_2 = 0.05$ eV, $M = 0$, and $\phi = \pi/2$) as a function $\hbar\omega$ for several incident angles $\psi = 0^\circ,\ 10^\circ,\ 20^\circ,\ 30^\circ$, and 30.42° ($\varepsilon_i = 3.9$, $\varepsilon_t = 1$).

spin-up electrons at the K' valley, while the LCP light is absorbed by the spin-up and the spin-down electrons at the K valley. The absorption spectra are given by the dashed and solid lines, which correspond to the excitations of electrons from the upper and the lower valence bands to the conduction bands, respectively. These spectra show the occurrence of VP.

We have demonstrated that the occurrences of CD and VP in the 2D hexagonal materials can be reproduced by using the Haldane model and show the roles of the intrinsic Hall conductivity in generating both phenomena. Thus, we have provided general formulas of the optical conductivities and absorption of circularly polarized lights in the 2D hexagonal materials with the broken $\mathcal{T}$ and $\mathcal{I}$ symmetries.

D. The Faraday and Kerr rotations in the topological Haldane material

In this subsection, we demonstrate the occurrence of the Faraday and Kerr rotations in the topological Haldane material. Unless otherwise specified, it is assumed that the 2D Haldane material with the parameters $t_2 = 0.05$ eV, $M = 0$, and $\phi = \pi/2$ is placed between a substrate ($\epsilon_i = 3.9$) and vacuum ($\epsilon_t = 1$). The introduction of the substrate is important to enhance the reflection probability [27]. In this system, the critical angle for incident light is $\psi_c = \arcsin(\sqrt{1/3.9}) = 30.42^\circ$, above which the total internal reflection occurs ($\psi \geqslant \psi_c$). We consider the incident light is linearly p polarized by putting $\xi_i \to 0$ in Eqs. (32) and (33). First, we calculate ξ_t and ξ_r as a function of the photon energy $\hbar\omega$ and the incident angle ψ. By using Eqs. (20) and (21), the Faraday and Kerr rotations are calculated. Hereafter, we adopt notations $\theta_t = \theta_F$ and $\theta_r = \theta_K$ to denote the Faraday and Kerr rotations, respectively.

Before discussing the Faraday and Kerr rotations, it is useful to recall the fact that linearly polarized incident light comprises the same number of left-handed and right-handed photons. Here we show CD as a function of ψ provides explanations of some results which shall be discussed. In Fig. 9, we separately plot the absorption probabilities of LCP and RCP lights for $\psi = 0^\circ,\ 10^\circ,\ 20^\circ,\ 30^\circ$, and 30.42°. The perfect CD occurs at $\hbar\omega = 0.52$ eV [corresponds to the energy gap of the topological Haldane material $\epsilon_g^{(\kappa)}$, see Fig. 4(a)] for $\psi = 0^\circ$ to $\psi = 20^\circ$. When the perfect CD occurs, ~4% of RCP ($\hat{\sigma} = -1$) light is absorbed and no absorption for the LCP light ($\hat{\sigma} = +1$). At the angle $\psi = 30^\circ$ partial CD is observed, because the absorption probability for LCP and RCP light are ~1% and ~3%, respectively. At the critical angle of incident ($\psi = 30.42^\circ$), CD vanishes, because LCP and RCP are absorbed equally by the Haldane material ($A \sim 2.6\%$).

The phenomenon shown in Fig. 9 can be explained by Eqs. (38)–(40), in which the absorption probability A consists of $A_p \propto \cos\chi[\cos\psi \mathrm{Re}(\sigma_{xx}\cos\chi + \xi_t\sigma_{xy})]$ and $A_s \propto [\cos\psi \mathrm{Re}(\sigma_{xx} - \sigma_{xy}\cos\chi/\xi_t)]$. At small incident angles ($\psi = 0^\circ$ to $\psi = 20^\circ$), $A_p \approx A_s \approx [\mathrm{Re}(\sigma_{xx}) - \hat{\sigma}\,\mathrm{Im}(\sigma_{xy})]$ [see Eq. (41)] in which perfect CD occurs. As ψ increases, χ becomes larger by the Snell law. Consequently, the contribution of the A_p term decreases. From Fig. 9, it is noted that for $\psi = 0^\circ - 20^\circ$, the change of A is not pronounced for both LCP and RCP lights, because the $\cos\chi$ does not vary significantly. At the critical angle, we have $\chi = 90^\circ$, and thus $A_p = 0$ and $A_s \propto [\cos\psi \mathrm{Re}(\sigma_{xx})]$. This means that A for both LCP and RCP lights only depend on the longitudinal conductivity $\sigma_{xx}(\omega)$ and not on the Hall conductivity $\sigma_{xy}(\omega)$. Since $\mathrm{Im}[\sigma_{xy}]$ is essential for CD, at the critical angle of incident CD can not occur.

In Fig. 10(a) we plot the Faraday rotation θ_F as a function of $\hbar\omega$ for $\psi = 0^\circ,\ 10^\circ,\ 20^\circ,\ 30^\circ$, and 30.42°. In the figure, it is observed that the Faraday rotation has a singular point at $\hbar\omega = \epsilon_g^{(\kappa)} = 0.52$ eV. In Fig. 10(b) the ellipticity of the transmitted light $\eta_t = \eta_F$ for the corresponding ψs are shown. Here the ellipticity suddenly increases when $\hbar\omega \geqslant \epsilon_g^{(\kappa)}$ and decreases for the higher photon energy. The origin of the singularities in θ_F and η_F can be explained by referring to Eq. (32). In the limit $\xi_i \to 0$, $\xi_t = \xi_F$ reduces to

$$\lim_{\xi_i \to 0} \xi_F = \frac{Z_i Z_t \sigma_{xy} \cos\chi}{\Delta_s}. \tag{48}$$

By substituting Eq. (48) into Eqs. (20) and (21), we have proportional relations $\theta_F \propto \mathrm{Re}[\sigma_{xy}]$ and $\eta_F \propto \mathrm{Im}[\sigma_{xy}]$. Therefore, the singularities in θ_F and η_F originate from the singular points in the real and imaginary parts of $\sigma_{xy}(\omega)$, respectively,

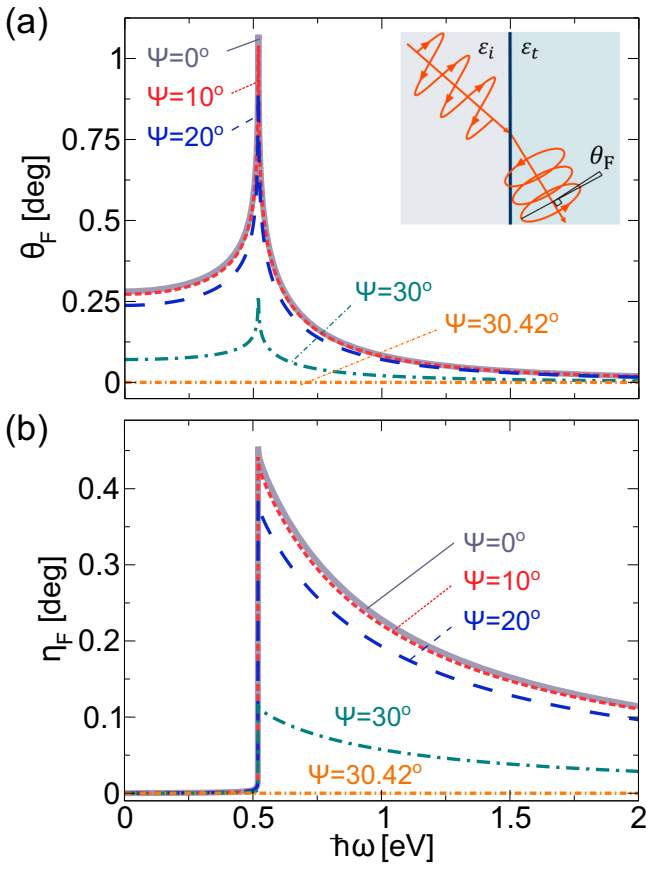

FIG. 10. (a) The Faraday rotation and (b) ellipticity of the transmitted light as a function of $\hbar\omega$ in the 2D Haldane material ($t_2 = 0.05$ eV, $M = 0$, and $\phi = \pi/2$) for several incident angles $\psi = 0°$, $10°$, $20°$, $30°$, and $30.42°$ ($\varepsilon_i = 3.9$, $\varepsilon_t = 1$).

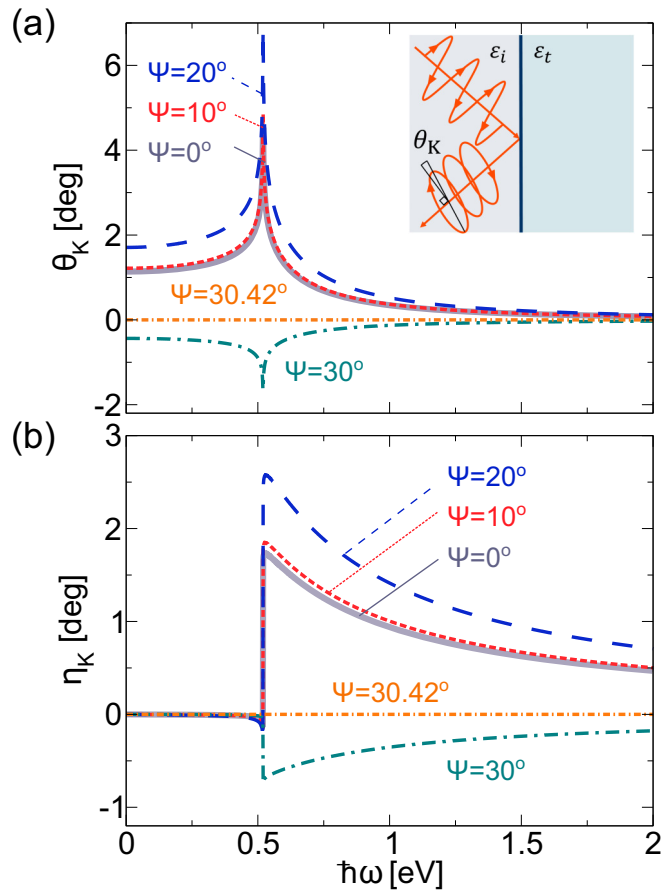

FIG. 11. (a) The Kerr rotation and (b) ellipticity of the reflected light as a function of $\hbar\omega$ in the 2D Haldane material ($t_2 = 0.05$ eV, $M = 0$, and $\phi = \pi/2$) for several incident angles $\psi = 0°$, $10°$, $20°$, $30°$, and $30.42°$ ($\varepsilon_i = 3.9$, $\varepsilon_t = 1$).

when the photon energy equal to the energy gap [see Figs. 4(a) and 4(b)].

The maximum $\theta_F \approx 1°$ is observed for the normal incident ($\psi = 0$), and θ_F decreases as ψ increases to ψ_c. This occurs because ξ_F is also proportional to $\cos\chi$. Hence, at the total internal reflection ($\chi = 90°$), there is no Faraday rotation ($\theta_F = 0$) since $\xi_F = 0$. As for the ellipticity of the transmitted light, it is shown that the largest $\eta_F \approx 0.45°$ is obtained at $\psi = 0$, which indicates that the transmitted light is almost linearly polarized. This occurs because only ~4% of the right-handed photons are absorbed, while there is no absorption for the left-handed photons (see Fig. 9). Therefore, after the transmission, the number of the left-handed photons is slightly higher than the right-handed ones, which implies positive ellipticity ($\eta_F > 0$) in the transmitted light. It can be shown that η_F is nonzero if there is CD. By using Eq. (41), the difference of A between LCP ($\hat{\sigma} = +1$) and RCP ($\hat{\sigma} = -1$) lights is given by

$$\mathrm{CD} = A_+ - A_- \propto -2\mathrm{Im}[\sigma_{xy}], \tag{49}$$

which is similar to the case η_F but has the opposite sign. Thus, when CD for LCP (RCP) light occurs, the transmitted light will acquires negative (positive) helicity. At $\psi = \psi_c = 30.42°$, the absorption probability LCP and RCP lights are equal as shown in Fig. 9, which implies that the transmitted light remains linearly polarized ($\eta_F = 0$).

In Figs. 11(a) and 11(b), we respectively plot the Kerr rotation θ_K and η_K as a function of $\hbar\omega$ for $\psi = 0°$, $10°$, $20°$, $30°$, and $30.42°$. Here again, singularities occur when the energy of photon is equal to the band gap, $\hbar\omega = \epsilon_g^\kappa = 0.52$ eV. However, at $\psi = 0°$ to $\psi = 20°$, both θ_K and η_K also increase, contrary to the previous case. We can see that the magnitudes of the Kerr rotation ($\theta_K \sim 4°$ to $6°$) are significantly larger than the Faraday rotation ($\theta_F \leqslant 1°$), and the reflected light is more elliptical (η_K up to $2°$) than that of the transmitted light ($\eta_F < 0.5°$). At $\psi = 30°$, θ_K and η_K become negative. This phenomenon can be explained by substituting $\xi_i \to 0$ and Eq. (48) into Eq. (32). In these limits, $\xi_r = \xi_K$ can be simplified as follows:

$$\lim_{\xi_i \to 0} \xi_K = \frac{Z_i Z_t \sigma_{xy} \cos\chi [1 + \Delta_s'/\Delta_s]}{\Delta_p' - [Z_i Z_t \sigma_{xy}]^2 \cos\psi \cos\chi/\Delta_s}. \tag{50}$$

The negative sign of ξ_K originates from the the fact that Δ_p' can be less than zero [see Eq. (36)], which means that the p components of the electric fields of the reflected and incident

lights have phase difference of π [27]. The direction of the Kerr rotation and the ellipticity of the transmitted lights are reversed, therefore $\theta_K < 0$ and $\eta_K < 0$. At the critical angle $\psi = 30.42^\circ$ ($\chi = 90^\circ$), $\xi_K = 0$. This implies that the reflected light does not undergo the rotation of polarization plane which gives the absence of the Kerr rotation ($\theta_K = 0$).

As a summary of this subsection, we have shown that the singularity of the real part of the Hall conductivity is essential to obtain large Faraday rotation (up to $\sim 1^\circ$) and Kerr rotation (up to $\sim 6^\circ$) in the topological Haldane material. The value of the Kerr rotation is comparable to that which is predicted by Széchenyi *et al.* for a gapped bilayer graphene (up to $\sim 6.5^\circ$), which possesses an intrinsic Hall conductivity due to the quantum anomalous Hall effect. However, it should be noted that the singularity of $\mathrm{Re}[\sigma_{xy}]$ only exists for the low temperature ($T \approx 0\ K$). At higher temperatures, the singularity becomes smeared and therefore the magnitudes of θ_F and θ_K would be smaller. In the trivial phase of the Haldane model, $\theta_F = 0$ and $\theta_K = 0$ because the Hall conductivities at the K and K' valleys have opposite signs, and, therefore, the Faraday and Kerr rotations can be used to detect the transition between the topological and the trivial cases in the Haldane material, as an alternative to wave-packet dynamics analysis as previously performed by Jotzu *et al.* [15,16].

IV. CONCLUSION

We analytically calculated the longitudinal and the Hall conductivities of the Haldane model. Our results can be applied for various 2D hexagonal materials with the broken $\mathcal{T}$ and $\mathcal{I}$ symmetries, in which electronic state of electron can be reproduced by the parameters t_2, ϕ, and M in the Haldane model. In particular, we have shown that the CD and VP in the 2D hexagonal materials depend on the imaginary part of the Hall conductivity. We also derived formulas for the Faraday and Kerr rotations in the Haldane model. The maximum magnitudes of the Faraday and Kerr rotations are obtained when the photon energy matches the band gap, due to the singularity of the real part of the Hall conductivity. Further, we have shown that the ellipticity of the transmitted lights is proportional to CD. Our treatment on the Faraday and Kerr rotations can also be applied for other 2D materials with intrinsic Hall conductivities.

ACKNOWLEDGMENT

F.R.P. acknowledges MEXT scholarship. M.S.U. acknowledges JSPS KAKENHI Grant No. JP18J10199. R.S. acknowledges JSPS KAKENHI Grant No. JP18H01810. We thank Dr. Sake Wang for useful discussion.

[1] K. S. Novoselov, A. K. Geim, S. V. Morozov, D. Jiang, Y. Zhang, S. V. Dubonos, I. V. Grigorieva, and A. A. Firsov, Science **306**, 666 (2004).
[2] A. H. Castro Neto, F. Guinea, N. M. R. Peres, N. S. Novoselov, and A. K. Geim, Rev. Mod. Phys. **81**, 109 (2009).
[3] M. Xu, T. Liang, M. Shi, and H. Chen, Chem. Rev. **113**, 3766 (2013).
[4] A. O. Govorov, Z. Fan, P. Hernandez, J. M. Slocik, and R. R. Naik, Nano Lett. **10**, 1374 (2010).
[5] A. B. Khanikaev, N. Arju, Z. Fan, D. Purtseladze, F. Lu, J. Lee, P. Sarriugarte, M. Schnell, R. Hillenbrand, M. A. Belkin, and G. Shvets, Nat. Commun. **7**, 12045 (2016).
[6] M. Ezawa, Phys. Rev. B **86**, 161407(R) (2012).
[7] K. F. Mak, K. He, J. Shan, and T. F. Heinz, Nat. Nanotechnol. **7**, 494 (2012).
[8] D. Xiao, G.-B. Liu, W. Feng, X. Xu, and W. Yao, Phys. Rev. Lett. **108**, 196802 (2012).
[9] T. Cao, G. Wang, W. Han, H. Ye, C. Zhu, J. Shi, Q. Niu, P. Tan, E. Wang, B. Liu, and J. Feng, Nat. Commun. **3**, 887 (2012).
[10] H. Zeng, J. Dai, W. Yao, D. Xiao, and X. Cui, Nat. Nanotechnol. **7**, 490 (2012).
[11] G. Kioseoglou, A. T. Hanbicki, M. Currie, A. L. Friedman, D. Gunlycke, and B. T. Jonker, Appl. Phys. Lett. **101**, 221907 (2012).
[12] S. Feng, C. Cong, S. Konabe, J. Zhang, J. Shang, Y. Chen, C. Zou, B. Cao, L. Wu, N. Peimyoo, B. Zhang, and T. Yu, Small **15**, 1805503 (2019).
[13] F. D. M. Haldane, Phys. Rev. Lett. **61**, 2015 (1988).
[14] D. Vanderbilt, *Berry Phases in Electronic Structure Theory* (Cambridge University Press, Cambridge, 2018).
[15] N. R. Cooper, J. Dalibard, and I. B. Spielman, Rev. Mod. Phys **91**, 015005 (2019).
[16] G. Jotzu, M. Messer, R. Desbuquois, M. Lebrat, T. Uehlinger, D. Greif, and T. Esslinger, Nature **515**, 237 (2014).
[17] H.-S. Kim and H.-Y. Kee, NPJ Quant. Mater. **2**, 1 (2017).
[18] K. Ghalamkari, Y. Tatsumi, and R. Saito, J. Phys. Soc. Jpn. **87**, 063708 (2018).
[19] I. Crassee, J. Levallois, A. L. Walter, M. Ostler, A. Bostwick, E. Rotenberg, T. Seyller, D. v. d. Marel, and A. B. Kuzmenko, Nat. Phys. **7**, 48 (2011).
[20] R. Shimano, G. Yumoto, J. Y. Yoo, R. Matsunaga, S. Tanabe, H. Hibino, T. Morimoto, and H. Aoki, Nat. Commun. **4**, 1841 (2013).
[21] B. Huang, G. Clark, E. Navarro-Moratalla, D. R. Klein, R. Cheng, K. L. Seyler, D. Zhong, E. Schmidgall, M. A. McGuire, D. H. Cobden, W. Yao, D. Xiao, P. Jarillo-Herrero, and X. Xu, Nature **546**, 270 (2017).
[22] G. Széchenyi, M. Vigh, A. Kormányos, and J. Cserti, J. Phys.: Condens. Matter **28**, 375802 (2016).
[23] Y. Ren, Z. Qiao, and Q. Niu, Rep. Prog. Phys. **79**, 066501 (2016).
[24] H. Bruus and K. Flensberg, *Many-Body Quantum Theory in Condensed Matter Physics* (Oxford University Press, Oxford, 2014).
[25] L. A. Falkovsky and A. A. Varlamov, Eur. Phys. J. B **56**, 281 (2007).
[26] E. Hecht, *Optics*, 5th ed. (Pearson, Boston, 2017).
[27] M. Born and E. Wolf, *Principles of Optics*, 7th ed. (Cambridge University Press, Cambridge, 2018).
[28] T. Stauber, N. M. R. Peres, and A. K. Geim, Phys. Rev. B **78**, 085432 (2008).
[29] M. S. Ukhtary, E. H. Hasdeo, A. R. T. Nugraha, and R. Saito, APEX **8**, 055102 (2012).

[30] Y. Harada, M. S. Ukhtary, M. Wang, S. K. Srinivasan, E. H. Hasdeo, A. R. T. Nugraha, G. T. Noe, II, Y. Sakai, R. Vajtai, P. M. Ajayan, R. Saito, and J. Kono, ACS Photon. **4**, 121 (2017).
[31] C.-C. Liu, W. Feng, and Y. Yao, Phys. Rev. Lett. **107**, 076802 (2011).
[32] C.-C. Liu, H. Jiang, and Y. Yao, Phys. Rev. B **84**, 195430 (2011).
[33] M. Ezawa, Phys. Rev. Lett. **109**, 055502 (2012).
[34] C. L. Kane and E. J. Mele, Phys. Rev. Lett. **95**, 226801 (2005).
[35] A. R. Wright, Sci. Rep. **3**, 2736 (2013).
[36] R. Yu, W. Zhang, H.-J. Zhang, S.-C. Zhang, X. Dai, and Z. Fang, Science **329**, 61 (2010).
[37] Z. Li and J. P. Carbotte, Phys. Rev. B **86**, 205425 (2012).